

## Research Article

# Experimental Research for CHF Sensitivity of Heat Flux Distribution under IVR Conditions

Shilei Han , Pengfei Liu , Bo Kuang, and Yanhua Yang

*School of Nuclear Science and Engineering, Shanghai Jiao Tong University, Shanghai 240200, China*

Correspondence should be addressed to Pengfei Liu; [pfliu@sjtu.edu.cn](mailto:pfliu@sjtu.edu.cn)

Received 15 November 2021; Accepted 18 February 2022; Published 16 March 2022

Academic Editor: Arkady Serikov

Copyright © 2022 Shilei Han et al. This is an open access article distributed under the Creative Commons Attribution License, which permits unrestricted use, distribution, and reproduction in any medium, provided the original work is properly cited.

In-vessel retention (IVR) through external reactor vessel cooling (ERVC) is one of the most effective severe accident mitigation measures in the nuclear power plants. The most influential issues on the IVR strategy are in-vessel core melt evolution, the heat fluxes imposed on the lower head, and the external cooling of reactor pressurized vessel (RPV). In the molten pool research, there are mainly two different molten pool configurations: two layers and three layers. Based on the different distributions of heat flux in molten pool configurations, a new problem was raised: whether the in-vessel heat flux distribution will affect the CHF on the outer wall of RPV and further affect the effectiveness of IVR measures? A full-height external reactor vessel cooling and natural circulating facility was conducted to study the CHF sensitivity of different heat flux distributions. The experimental results show that the characteristics of natural circulation are similar and the CHF of the RPV lower head external surface is not obviously affected under the different heat flux distributions. The varying heat flux distribution during severe accident process will not threaten significantly the success of IVR strategy.

## 1. Introduction

Nuclear power safety involves estimation of the radiation risks to public and the efforts to reduce these risks. After the Fukushima Daiichi accident, the improvements of nuclear power plants to enhance the mitigation capability have been more essential and urgent. The IVR strategy is one of the considered modification actions for pressurized water reactor (PWR).

During the severe accident process, the cooling water is lost and the reactor core is lack in coolant. Then, the temperature of reactor core increases and is over the melting point. The molten material relocates in the RPV lower plenum. In the lower head of RPV, without severe accident mitigation measures, the molten pool is lack in coolant and heating the RPV wall. As the wall temperature increases, the RPV wall is penetrated by the molten material. The integrity of RPV will be broken. To avoid the leakage of radioactive material, the IVR strategy is proposed. The IVR strategy aims to keep the molten material inside the RPV by external cooling outside the lower head wall.

The IVR strategy has been studied for a long time [1] and originated from the Loviisa VVER-440 in Finland in order to cope with the core-melt risk [2] and then was adopted in the Westinghouse reactor AP600 [3]. Then, the IVR strategy is employed in the newly designed reactors such as AP1000, APR1400, HPR1000, and so on [4–8].

Figure 1 is the schematic diagram of IVR. The molten material of reactor core is finally relocated in the lower head and forms a molten pool heated by the decay heat. The coolant flow (normally driven by natural circulation in passive safety features) through the external surface of RPV cools down the lower head. With ERVC, the temperature will be kept in the safety margin to avoid the meltdown of RPV.

The key point of IVR strategy is that the decay heat of the molten pool can be removed by the coolant flow. This requires that the angular heat flux imposed by the molten pool to the lower head cannot exceed the capacity of external cooling, that is, the critical heat flux (CHF) at all points on the lower head. Otherwise, the integrity of the vessel will be lost, sooner or later, due to a boiling crisis and subsequent

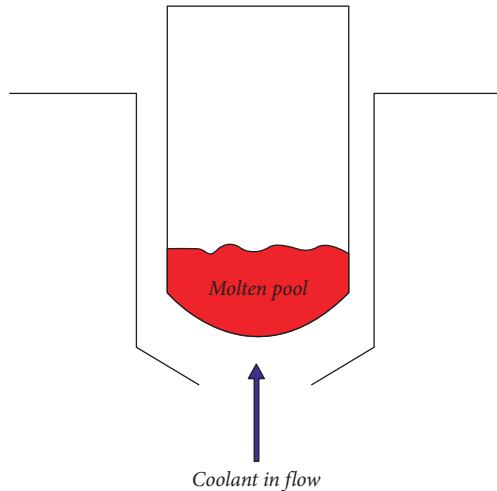


FIGURE 1: Schematic diagram of IVR.

escalation of vessel wall temperature. Although the purpose of IVR strategy is simple, there is still some difficulty for the implementation of IVR strategy. The challenge is that the imposed heat flux is largely affected by the in-vessel severe accident phenomena and accident scenarios. Because of the uncertainties in the physical phenomena and accident scenarios, the IVR strategy should consider more details and probabilities during severe accident process. The most influential issues on the IVR strategy are in-vessel core melt evolution, the heat fluxes imposed on the lower head, and the external cooling of RPV. During the severe accident, the reactor core is exposed and then the core degradation occurs. The core is molten and relocates in the RPV lower plenum. The molten pool (mixture of core materials:  $\text{UO}_2$ , Zr, Fe, and so on) is formed in the lower plenum.

In the previous IVR analysis, it is focused on the two-layer molten pool, as shown in Figure 2(a). There is a metal layer over the oxide layer. The RASPLAV project [9] found that materials such as carbon had a strong influence on the molten pool stratification. Moreover, it has been proved in the MASCA project [10] that the addition of steel to U-Zr-O mixtures can result in an inversely stratified state due to the density inversion. The molten heavy metal stratifies below the oxide layer. The density of uranium metal is higher than that of  $\text{UO}_2$  and other oxides. Therefore, when some uranium of  $\text{UO}_2$  is reduced and transferred into the metal layer, the density inversion may occur and the heavy metal layer is formed. The three-layer configuration is shown in Figure 2(b). Because of the transfer of uranium metal, the mass of metal layer is reduced and this light metal layer gets thinner, which leads to a focus effect of the heat flux. This focus effect could reduce the safety margin of IVR strategy and threaten the integrity of the RPV.

In the effectiveness calculation of IVR in AP600 done by INEEL [11], several transients which had different heat flux distributions were shown. During the process of core melt accident, the steady and transient states in the lower head are complex and the distribution of heat flux toward the lower head wall is varying. Some researchers have argued that there is a theory that upstream heat flux

distributions affect the bubble layer at the boiling crisis position, while one investigator has found that there is no correction factor of CHF prediction between uniform heating and nonuniform heating [12]. Therefore, it is necessary to consider the effects of heat flux distribution on the local flow characteristics, heat transfer, and CHF to identify whether the varying heat flux distribution threatens the integrity of RPV.

## 2. Experimental Facility and Procedure

The downward-facing surface heating and flow boiling experimental facility is constructed to conduct the full-size tests of CHF on lower head external wall for IVR strategy [13–15]. Several auxiliary systems are prepared to help conduct the experiments successfully. In this paper, the effect of heat flux distribution is focused. The related CHF experiments are conducted to study the CHF sensitivity of heat flux distribution.

**2.1. Natural Circulation Loop and Heating Block.** As shown in Figure 3, flow boiling CHF experiments are conducted in the natural circulation loop. The flow is driven by the density difference between upward water tank (f) and flow passage in test section (d). Referring to the overall and detailed configuration and parameters of prototypic ERVC in the NPP, the facility has been constructed to simulate the features and flow characteristics of prototypic ERVC. The following requirements are satisfied:

- (1) One-dimensional full-height facility, with 1 : 1 height ratio of each model section to its prototype
- (2) 1 : 100 ratio for the important flow passage cross-section areas
- (3) A complete geometric simulation of ERVC flow channel between RPV wall and insulation layer
- (4) A simulation design of inlet and outlet conditions of ERVC flow
- (5) The facility has the capability of simulating the ERVC process under some real conditions in NPP, such as nonuniform heating, RPV surface aging, and sub-cooling of fluids

The flow loop is divided into two parts: single-phase part and two-phase part. The modelling for these two parts is conducted, respectively. In Figure 4, the flow passage is the two-phase part in this loop. Along the flow direction, the bubbles are accumulated. The angular  $\theta$  of flow passage is from 0 to 90°. In the CHF experiments, 27°, 42°, 57°, 72°, 81°, and 87° are chosen as test cases. The temperatures and pressure drops are measured.

The heat section is designed as two different kinds: Cu and explosive welding Cu-steel. Several hundred heating rods are inserted into the Cu section as heating power. Maximum heat flux can reach to 2.2 MW/m<sup>2</sup>. Three N-type thermocouples are settled at the heater at each degree, and three T-type thermocouples are settled in the flow passage at each 15°.

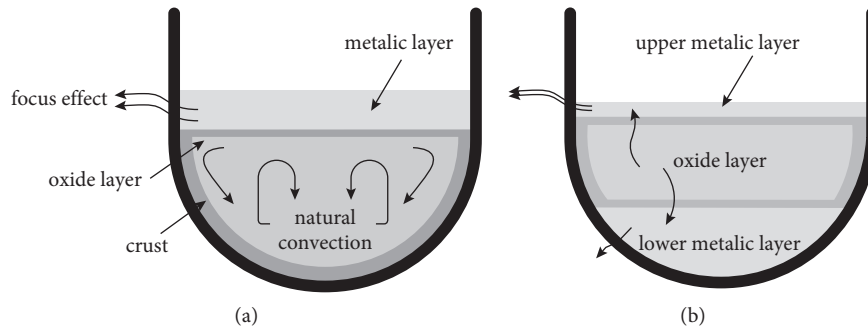


FIGURE 2: Molten pool configurations: (a) two layers and (b) three layers.

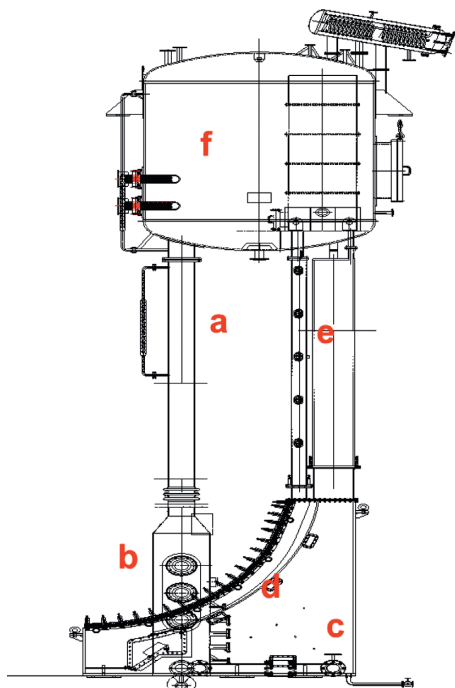


FIGURE 3: Natural circulation loop of CHF experiments, where a is the downward pipe, b is the inlet water chamber, c is the downward water tank, d is the flow passage heated by heat section, e is the upward pipe, and f is the upward water tank.

Besides the main experimental facilities, several support systems are set to make the experiments conducted successfully. These systems consist of deionized water making system, preheating system, pressure control system, chemical control system, condensation and cooling system, and wastewater treatment system.

**2.2. Calculation of Heat Flux Distribution.** In the IVR analysis, one of the important issues is the heat flux boundary condition toward the lower head wall. To get the heat flux distribution, much work has been done to model the molten pool and calculate the heat flux.

SPIRE is a modular IVR analysis program designed for molten pool heat transfer and CHF calculation [16]. The metal layer in two-layer molten pool is from 71° to 84°, while the

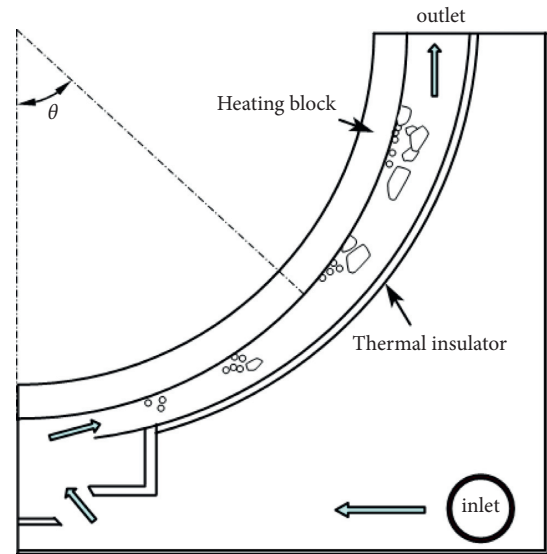


FIGURE 4: Flow passage diagram.

light metal layer in three-layer molten pool is from 74° to 85°. Figure 5 shows the two heat flux distributions calculated by SPIRE. The three-layer molten pool has an obviously different heat flux distribution compared to the two-layer molten pool. In the three-layer molten pool, the metal material in the top layer is transferred into the heavy metal layer at the bottom. Therefore, the light metal layer gets thinner and leads to a thermal focus effect, which may threaten the integrity of RPV. According to the results of molten pool research studies conducted by Ge et al. and Zhou et al. [17, 18], the calculation results of SPIRE are reasonable. In the IVR evaluation for Chinese improved 1000<sup>o</sup>MWe PWR [19], the heat flux distribution of three-layer molten pool has been calculated. There is a focus effect of heat flux at about 80°, which is similar to the results of SPIRE.

According to the actual heat flux distribution in prototype molten pool calculated by programs, the boundary condition of heat flux in the experiments can be set. However, for the experimental design, it is difficult to simulate the three-dimensional heat flux distribution. As the lower head is axially symmetric, it is reasonable to study the flap-like part. However, this flap-like heater will still bring some difficulty in the experiments. Therefore, the heater in

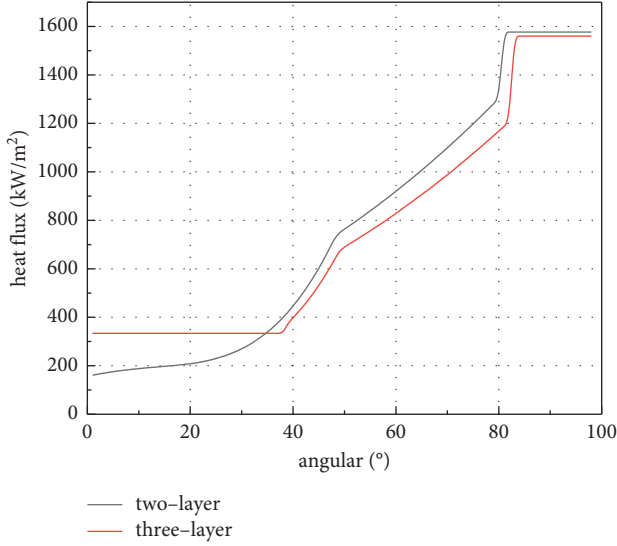


FIGURE 5: Heat flux distributions calculated by SPIRE.

this experiment is aquilate. Because of the difference between flap-like and aquilate heaters, the heat flux distribution needs to be equivalently converted. Besides, the upstream and downstream conditions of prototype and model should be equivalent. Therefore, two requirements are needed to be satisfied:

- (1) For  $\theta < \theta_m$  ( $\theta_m$  is the test angular), the bubbles are accumulated from the inlet of flow passage so that at  $\theta = \theta_m$ , the similar flow rate can be reached and the two-phase boundary layer is formed at upstream region. Finally, the condition at upstream region is similar to that in prototype.
- (2) During ERVC process, the fluid near external lower head surface is heated and evaporated. The bubbles are generated, departed, collided, broken, and moved with mainstream. As the heat flux increases, the generation rate of bubbles increases. When the surface is covered by bubbles and the heating power cannot be removed by water, the boiling crisis occurs. This means that the superficial velocity of bubbles needs to be similar to that of the prototype at downstream region. Therefore, for  $\theta > \theta_m$ , the superficial velocity of bubbles is similar to that of the prototype.

Theofanous proposed a method of local modelling based on the two-dimensional distribution in the ULPU experiments [1]. Referring to the method of Theofanous, the heat flux in experimental model  $q_e(\theta)$  can be conducted:

$$q_e(\theta) = \begin{cases} q_p(\theta) \frac{\sin \theta}{\sin \theta_m}, & \theta < \theta_m, \\ q_p(\theta) - \frac{\cos \theta}{\sin^2 \theta} \int_0^\theta q_p(\theta') \sin \theta' d\theta', & \theta > \theta_m, \end{cases} \quad (1)$$

where  $q_p(\theta)$  is the heat flux distribution of prototype lower head and  $\theta_m$  is the test angle where the heat flux is maximum.

For the two-layer and three-layer molten pool experiments, the heat flux distributions are calculated by (1) shown in Table 1. For the heat flux distribution code “SF-nn-0.x,” “SF” means shaped heat flux distribution, “nn” means the test angular, and “0.x” means that the downward heat flux calculated by the equations is multiplied by 0.x to make sure the CHF is approached at the test angular.

In the normalized heat flux factor distribution figures, three-layer molten pool has a higher upstream heating power  $P_{upstream}$  than two-layer molten pool for 27°, 42°, 57°, 72°, and 81° cases. As for the 87° case, the upstream heating power is lower in three-layer molten pool because of the focus effect at high angular (over 80°).

**2.3. Experimental Procedure.** To study the effect of molten pool configurations on CHF in lower head, the related CHF experiments were conducted. Besides, considering the complex heat flux distribution in prototype molten pool, the effects of upstream and downstream heating powers,  $P_{upstream}$  and  $P_{downstream}$ , were also studied in the series of CHF experiments. The detailed test matrix is shown in Table 2. The heat flux factor distributions in test cases 2 and 3 are shown in Figure 6.

During the experimental process, the deionized water is pumped into the preheating system to be heated up to the required temperature. Then, the water is pumped into the natural circulation loop to be prepared for the experiment. Next, the heating power is increased step by step until the CHF phenomenon occurs. During this process, the condensation and cooling system is used to keep the water at the required temperature so that during the total experimental process, the temperature of water is almost constant (fluctuates within 1°C). The CHF phenomenon is distinguished by the temperature leap of the thermocouples, and then the heating power is cut down manually to prevent the Cu-steel overheated.

The identification of boiling crisis is the essential step during the experimental process. As the heating power increases step by step during the tests, the phenomenon can be observed by the temperature jump in the data acquisition system such as shown in Figure 7. When the temperatures of a/b/c thermocouples have some increase in unit time (e.g., 20°C, 30°C, and 40°C) without change of the heating power, which means the heating block and circulation are under transition state, it is identified that boiling crisis occurs.

To ensure that the heat flux when temperature jump occurs is CHF, the heating power is reduced and increased step by step until temperature jump occurs again. When the heating power is close to the value of first temperature jump, the increase step is reduced to a half.

**2.4. Data Processing.** When heating power is close to the value that may cause temperature jump, the increase step is reduced to the minimum power that the heating controller can distinguish.

The CHF value can be calculated by

TABLE 1: Heat flux distributions for different molten pool configurations.

Heat flux distribution code	Normalized factor distribution figure	Remark
SF-27-0.1	<p>The graph for SF-27-0.1 shows the normalized heat flux factor on the y-axis (0.0 to 1.0) against the angular degree on the x-axis (0 to 80). Two curves are plotted: a black line for the two-layer configuration and a red line for the three-layer configuration. Both curves show a sharp peak at approximately 27 degrees, where the heat flux factor reaches 1.0. The three-layer curve remains at 1.0 for a slightly wider range around the peak compared to the two-layer curve.</p>	$\theta_m = 27^\circ$
SF-42-0.2	<p>The graph for SF-42-0.2 shows the normalized heat flux factor on the y-axis (0.0 to 1.0) against the angular degree on the x-axis (0 to 80). Two curves are plotted: a black line for the two-layer configuration and a red line for the three-layer configuration. Both curves show a sharp peak at approximately 42 degrees, where the heat flux factor reaches 1.0. The three-layer curve remains at 1.0 for a wider range around the peak compared to the two-layer curve.</p>	$\theta_m = 42^\circ$
SF-57-0.5/0.4	<p>The graph for SF-57-0.5/0.4 shows the normalized heat flux factor on the y-axis (0.0 to 1.0) against the angular degree on the x-axis (0 to 80). Two curves are plotted: a black line for the two-layer configuration and a red line for the three-layer configuration. Both curves show a sharp peak at approximately 57 degrees, where the heat flux factor reaches 1.0. The three-layer curve remains at 1.0 for a wider range around the peak compared to the two-layer curve.</p>	$\theta_m = 57^\circ$
SF-72-0.5	<p>The graph for SF-72-0.5 shows the normalized heat flux factor on the y-axis (0.0 to 1.0) against the angular degree on the x-axis (0 to 80). Two curves are plotted: a black line for the two-layer configuration and a red line for the three-layer configuration. Both curves show a sharp peak at approximately 72 degrees, where the heat flux factor reaches 1.0. The three-layer curve remains at 1.0 for a wider range around the peak compared to the two-layer curve.</p>	$\theta_m = 72^\circ$

TABLE 1: Continued.

Heat flux distribution code	Normalized factor distribution figure	Remark
SF-81-0.5		$\theta_m = 81^\circ$
SF-87-0.5		$\theta_m = 87^\circ$

TABLE 2: Test matrix.

Test case	Natural circulating height (m)	Pressure (bar)	Inlet water temperature ( $^\circ\text{C}$ )	Power shape	Test angular ( $^\circ$ )
1	8	1	100	Two-layer	27,42,57 72,81,87
2	8	1	100	Two-layer $P_{upstream} \times 0.6, 0.7, 0.8$	72
3	8	1	100	Two-layer $P_{downstream} \times 0.3, 0.4, 0.6, 0.7$	72
4	8	1	100	Three-layer	27,42,57 72,81,87

$$q_{\text{CHF}} = \left( \frac{P_{\text{CHF},i}}{S_i} \right) \cdot C = q_{\text{CHF,apparent}} \cdot C, \quad (2)$$

where  $P_{\text{CHF},i}$  and  $S_i$  are the heating power when CHF is approached and boiling surface area at the angle corresponding to the heat power  $P_i$ .  $C$  is a correction factor caused by the circumferential heat conduction and heat leakage in the nonuniform heating block. The factor  $C$  is defined by

$$C = \frac{q_{\text{actual}}}{q_{\text{input}}}. \quad (3)$$

$q_{\text{actual}}$  is the actual CHF which can be determined by the thermal equilibrium of the heating block. The thermal equilibrium of heating block is shown in Figure 8.  $P_i$  is the

input heating power of the  $i$ th group heat rods.  $q_{uw}$ ,  $q_{sw}$ , and  $q_{stw}$  are heat leakages through thermal insulation from upper surface, side surface, and supporting surface.  $q_l$  and  $q_r$  are the circumferential heat conduction. These heat fluxes are calculated by Fourier's law using the temperature of thermocouples arranged on heating block wall.  $q_B$  is the boiling heat transfer between the wall and fluid.

The initial conditions and boundary conditions are input for the thermal equilibrium analysis. As for  $q_B$ , the heat transfer coefficient  $h$  is set as an assumed initial value. By fixing the value of  $h$ , the calculated temperature field is close to that measured by a/b/c thermocouples (the error is less than  $2^\circ\text{C}$ ). Therefore, the maximum value of  $q_B$  on the convective heat transfer surface is the value of CHF,  $q_{\text{CHF}}$ .

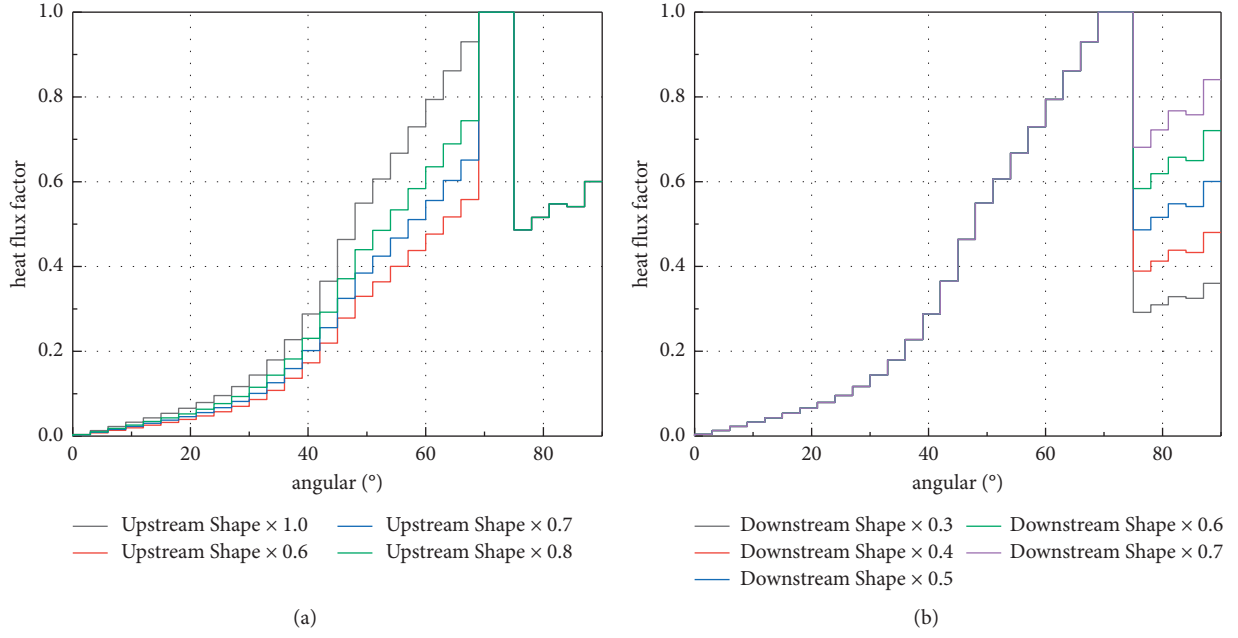


FIGURE 6: Heat flux distributions of (a) test case 2 and (b) test case 3.

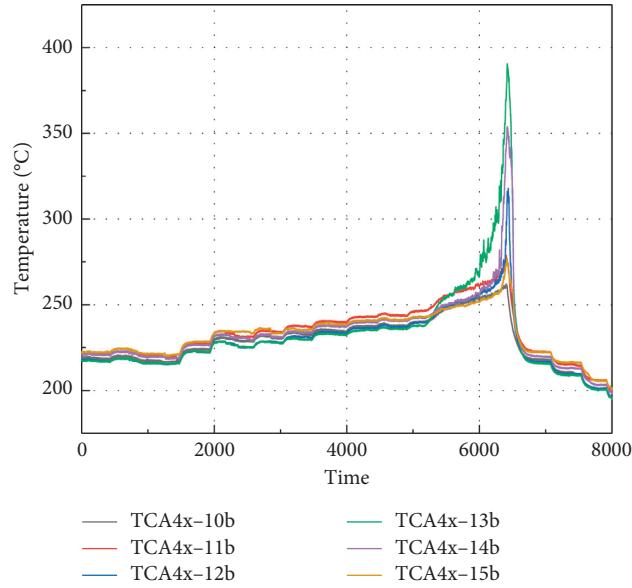


FIGURE 7: Example of temperature jump when CHF is approached.

Since  $q_{\text{CHF}}$  is obtained indirectly, the uncertainty analysis of  $q_{\text{CHF}}$  is conducted by

$$\begin{aligned}
 \delta q_{\text{CHF}} &= \delta f(q_{uw}, q_{sw}, q_{stw}; P_{11}, \dots, P_{15}; \varepsilon_1, \dots, \varepsilon_{15}) \\
 &= \sqrt{\left(\frac{\partial f}{\partial q_{uw}}\right)^2 (\delta q_{uw})^2 + \left(\frac{\partial f}{\partial q_{sw}}\right)^2 (\delta q_{sw})^2 + \left(\frac{\partial f}{\partial q_{stw}}\right)^2 (\delta q_{stw})^2 + \sum_{i=11}^{15} \left[\left(\frac{\partial f}{\partial P_i}\right)^2 (\delta P_i)^2\right]} \\
 &\quad + \sum_{k=1}^{15} \left[\left(\frac{\partial f}{\partial \varepsilon_k}\right)^2 (\delta \varepsilon_k)^2\right] + \left(\frac{\partial f}{\partial q_l}\right)^2 (\delta q_l)^2 + \left(\frac{\partial f}{\partial q_r}\right)^2 (\delta q_r)^2,
 \end{aligned} \tag{4}$$

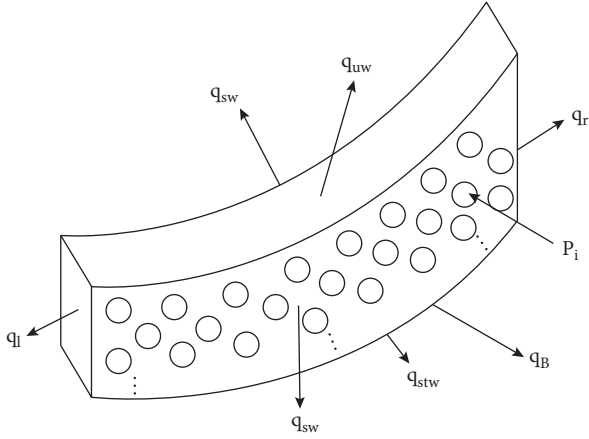


FIGURE 8: Scheme of thermal equilibrium of heating block.

where  $\varepsilon_k$  is the difference of temperatures of calculation and thermocouples.

Based on the single variable method,  $q_{uw}$ ,  $q_{sw}$ ,  $q_{stw}$ ,  $P_i$ ,  $q_l$ ,  $q_r$ , and  $h$  are changed, respectively, to get the maximum heat flux. The changes in variables aim to reduce the maximum heat flux. By linear fitting of heat flux and variables, the sensitivity coefficient  $\partial f/\partial X$  is obtained. The disturbance variable  $\partial X$  is dependent on the uncertainty of thermocouples  $\delta\varepsilon$  ( $\delta\varepsilon = 0.95^\circ\text{C}$ ) and uncertainty of heating power  $\delta P$  ( $\delta P = 0.6697 \text{ W}$ ). Each region of heating block is divided into 15 parts. The disturbance variable  $\partial\varepsilon_k$  is dependent on convergence condition (the temperature difference between calculation results and measurement results is less than  $2^\circ\text{C}$ ) and the uncertainty of thermocouples  $\delta\varepsilon$ .

With all the above analyses,  $q_{CHF}$  can be obtained by

$$q_{CHF} = q_{CHF,apparent} \pm \delta q_{CHF}. \quad (5)$$

### 3. Results and Discussion

**3.1. Effect of Heat Flux Distribution on Flow Characteristics.** During the different severe accident processes, especially different relocation processes, there will be different heat flux distributions in the lower head. This issue may affect the flow characteristics, such as driving force of natural circulation. To comprehensively study the effect on flow characteristics, two total heating powers  $P_{total}$  170 kW and 300 kW are chosen in the test case 1. When  $P_{total} = 170 \text{ kW}$ , the natural circulation is under instable state; when  $P_{total} = 300 \text{ kW}$ , the natural circulation is under steady state.

Figures 9 and 10 show the pressure drops between the both sides of insulator (DP1001( $\theta = 30^\circ$ ), DP1002( $\theta = 60^\circ$ ), DP1003 ( $\theta = 80^\circ$ ), and DP1003 A ( $\theta = 88^\circ$ )). When  $P_{total} = 170 \text{ kW}$ , the natural circulation is under instable state for the different power shapes. The flow rate, pressure, and pressure drop are in low frequency oscillation (about 0.03–0.3 Hz), while there is a relatively high frequency and small amplitude oscillation (about 1.7 Hz) caused by the boiling and condensation in the natural circulation loop. When  $P_{total}$  is increased to 300 kW, the natural circulation is under steady state. The low frequency oscillation disappears

and the flow is in the relatively high frequency and small amplitude oscillation (about 1.7 Hz). There is only little difference of values of pressure drops (about 0.3–0.4 kPa) for different power shapes.

In general, the flow characteristics are barely influenced by the power shape.

**3.2. The Effect of Upstream and Downstream Heating Power on CHF.** In the experiments of upstream and downstream heating power, the power shapes shown in Figure 6 are used. Figure 11 gives the CHF results. It is obvious that the CHF is not influenced by the power shapes of upstream and downstream. The reduced  $P_{upstream}$  leads to a higher peak heating power which means a larger  $q_{CHF,apparent}$ . However, after the thermal equilibrium calculation, the difference of  $q_{CHF}$  is less than 5%.  $P_{downstream}$  has a less effect on CHF (less than 1%). The boiling crisis is approached by the bubble accumulations in upstream and the local heat flux.  $P_{downstream}$  cannot influence the bubble behaviour in upstream. When  $P_{upstream}$  is reduced, the bubbles from the upstream are reduced and there will be more heat flux from the peak heating power region to the upstream region. Therefore, a larger heating power is needed to reach the similar bubble behaviour and the same heat flux at the test position.

The boiling crisis is mainly dependent on the local heat flux and barely affected by  $P_{upstream}$  and  $P_{downstream}$ .

**3.3. Effect of Molten Pool Stratification.** Considering that the different heat flux distributions may change the process of bubble accumulation along the flow passage, the test cases 1 and 4 could have different two-phase flow characteristics. Figure 11 gives the relation of flow rate and total heating power (THP). The curves in Figure 12 have the same trend. The flow characteristics of natural circulation are not affected by the molten pool configurations. Besides, Figure 13 shows the same pressure drop between inlet and outlet of flow passage in tests 1 and 4.

Because of the different configurations of three-layer molten pool,  $P_{total}$  and  $P_{upstream}$  are larger than those of two-layer molten pool with the same maximum heat flux at test angular. This leads to a smaller circumferential temperature gradient of the heating block (Cu-steel) and a lower  $q_{CHF,apparent}$  (SF-87-0.5 is the exception because of the focus effect). After thermal equilibrium calculation, the results shown in Figure 14 are similar. The relative deviations of these two series of  $q_{CHF}$  are less than 3%, as shown in Figure 15. Only the  $q_{CHF}$  of  $81^\circ$  and  $87^\circ$  cases in test 4 are lower than those in test 1. However, the focus effect did not greatly affect the CHF at this region. The CHF is higher than the imposed heat flux distributions of two different molten pools.

**3.4. Comparison of the SF-72-0.5 Case with T40B in ULPU-V.** In this paper, the experiments of two-layer molten pool are compared with the ULPU-V experiments [20]. The power shape of test angular  $70^\circ$  is chosen, which is SF-72-0.5 in this



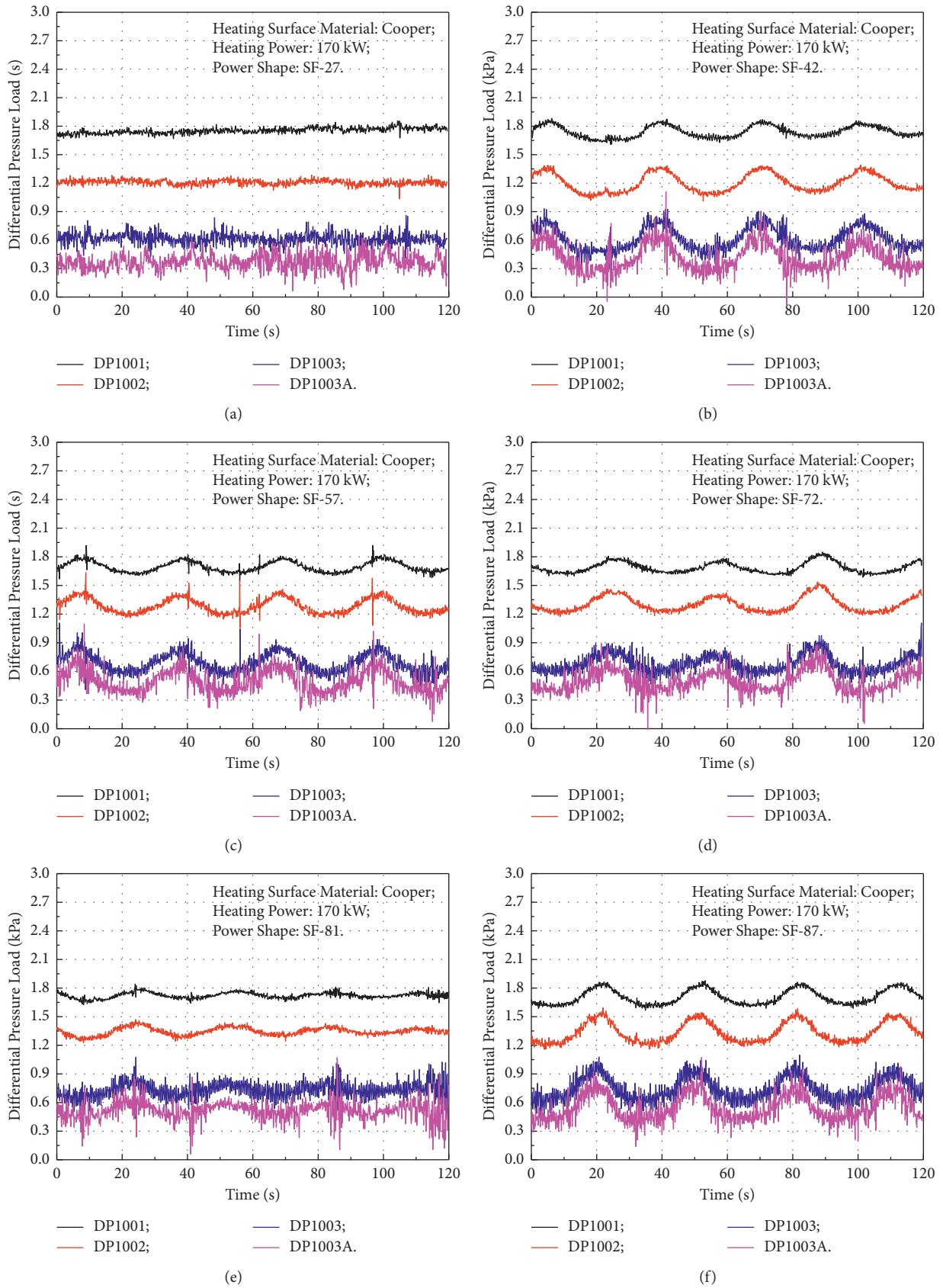


FIGURE 9: Pressure drops when  $P_{total} = 170kW$ . (a) SF-27. (b) SF-42. (c) SF-57. (d) SF-72. (e) SF-81. (f) SF-87.

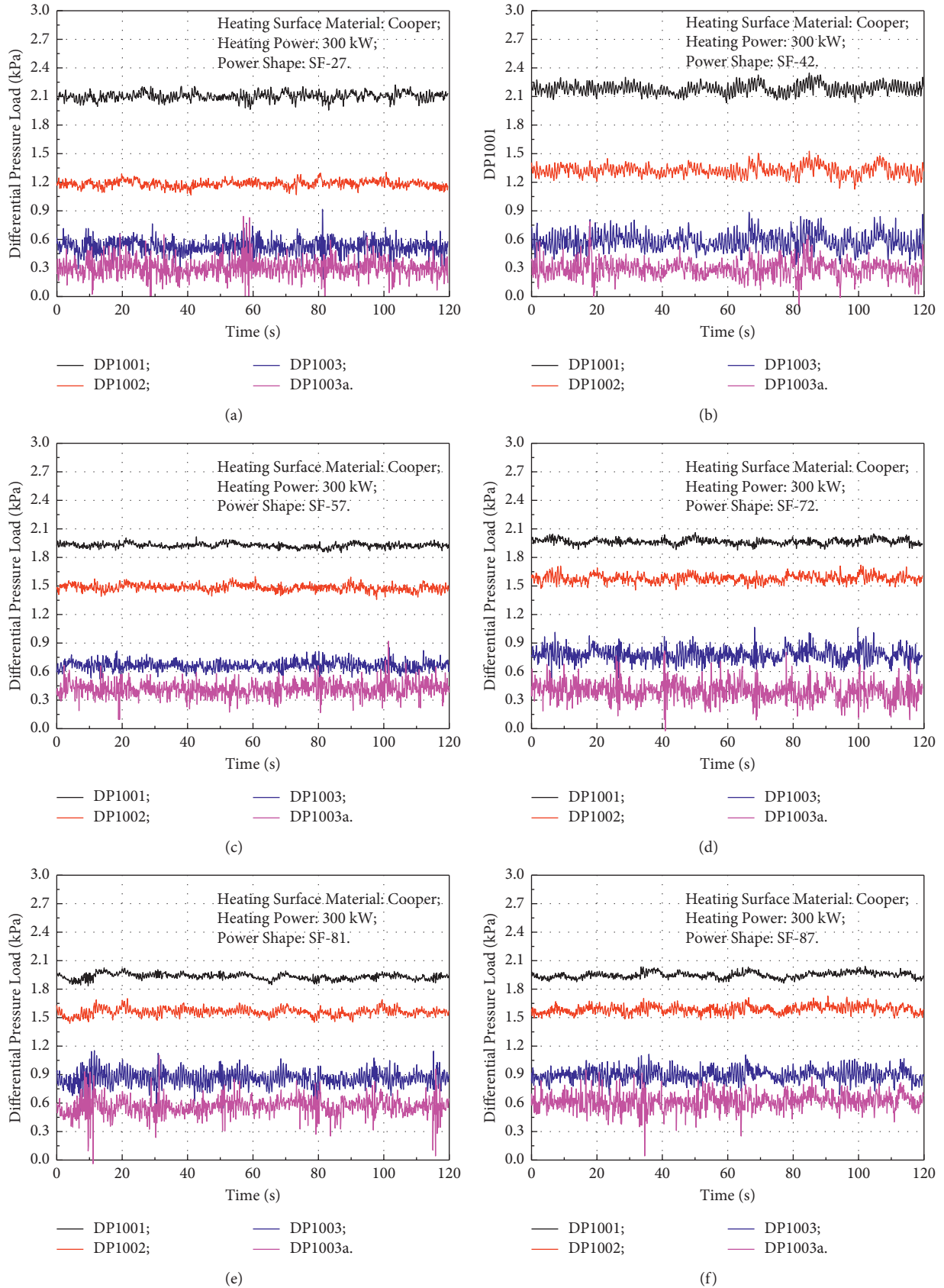


FIGURE 10: Pressure drops when  $P_{total} = 300kW$ . (a) SF-27. (b) SF-42. (c) SF-57. (d) SF-72. (e) SF-81. (f) SF-87.

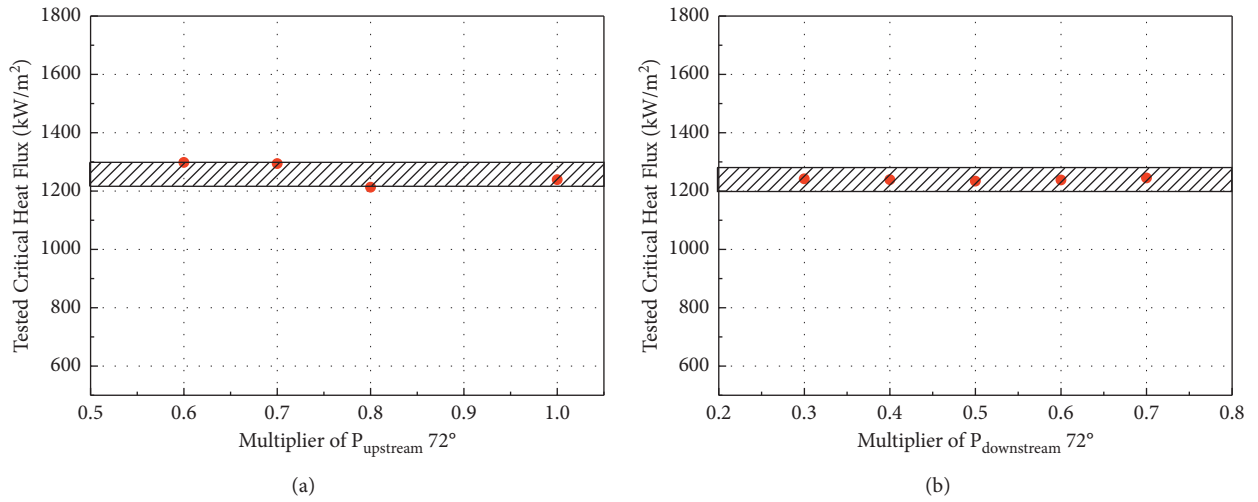


FIGURE 11: CHF results of upstream and downstream heating power experiments. (a) Test case 2. (b) Test case 3.

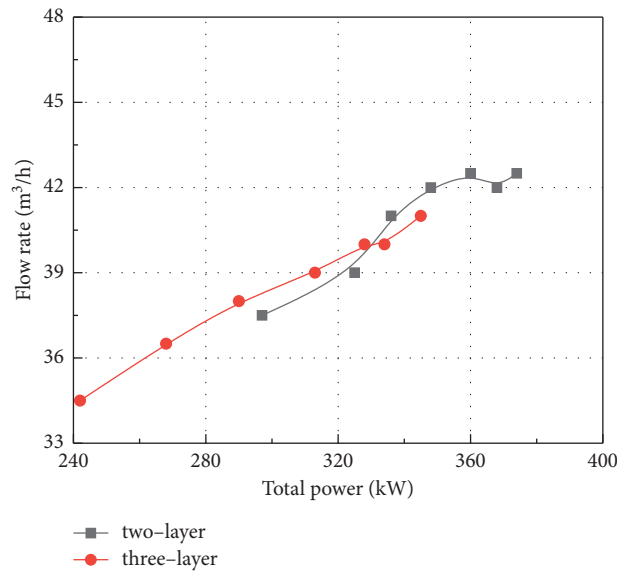


FIGURE 12: Variation of flow rate with THP.

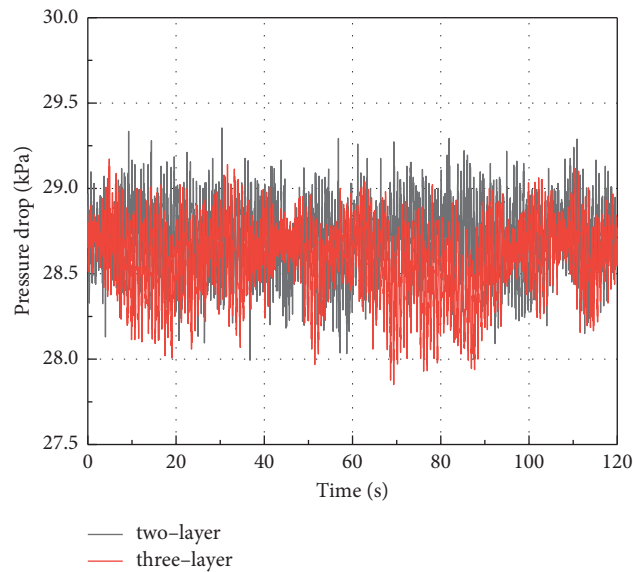


FIGURE 13: Pressure drop between the inlet and outlet of flow passage at  $q = 1600 \text{ kW/m}^2$ .

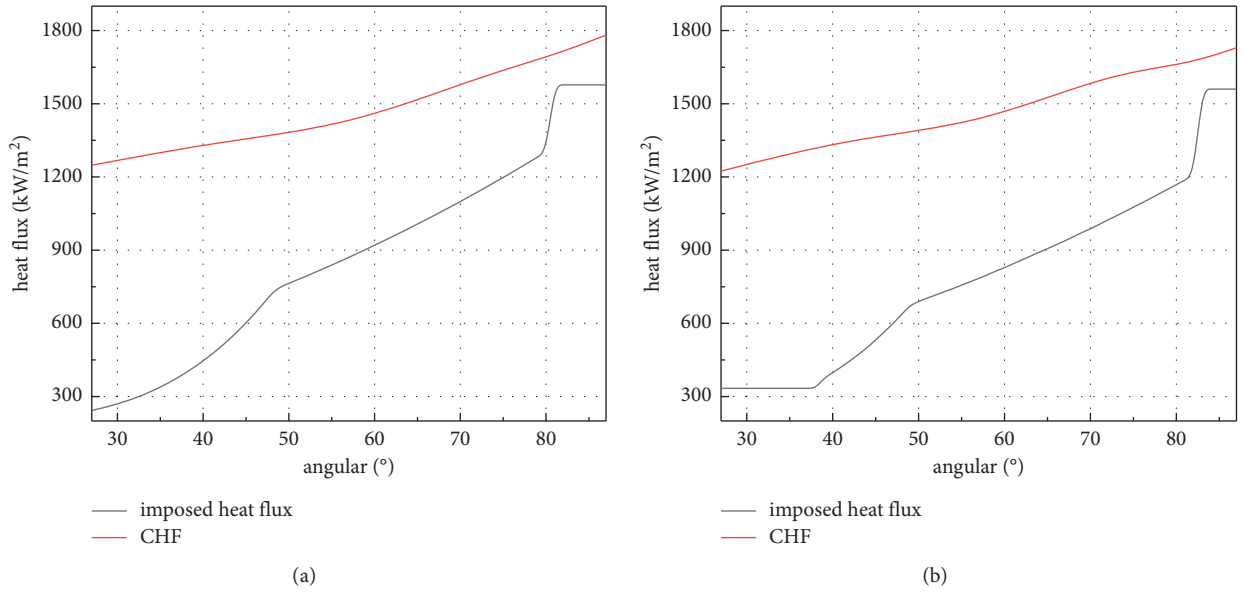


FIGURE 14: CHF compared with imposed heat flux in tests 1 and 4. (a) Two-layer. (b) Three-layer.

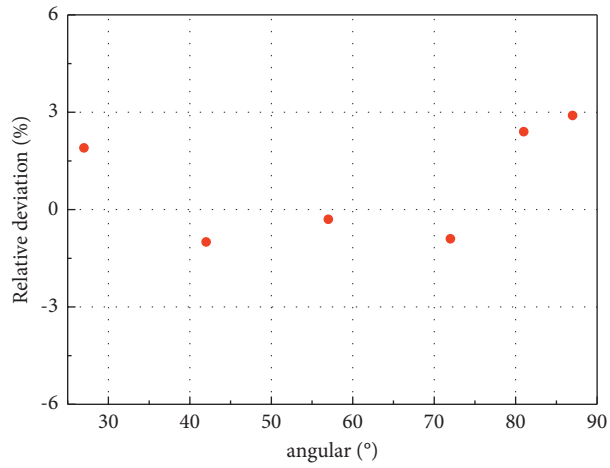


FIGURE 15: Relative deviations of  $q_{CHF}$  in tests 1 and 4.

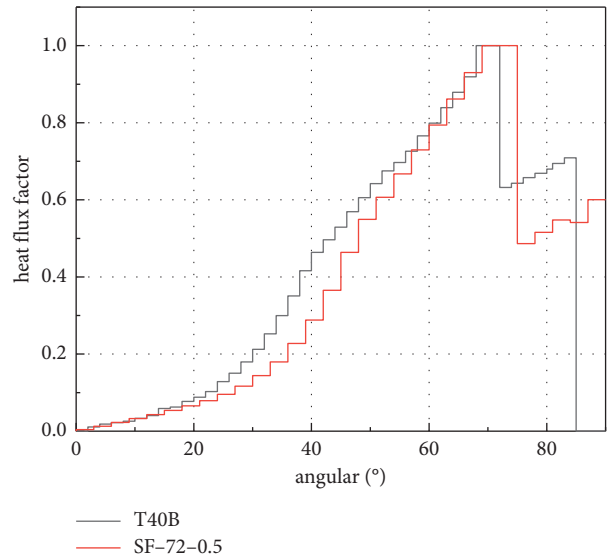


FIGURE 16: Power shape of T40B and SF-72-0.5.

TABLE 3: Comparison of SF-72-0.5 and T40B.

Test case	SF-72-0.5	T40B (ULPU-V)
CHF (kW/m <sup>2</sup> )	1449	1453
Flow rate (m <sup>3</sup> /h)	38.2	39.0
Pressure drop between inlet and outlet (kPa)	23.95	14.99
Total power (kW)	332	187
Power percentage at 85°–90°	12%	0
Total power at 0–84° (kW)	208.6	187

paper and T40B in ULPU-V. Compared with the power shape in Figure 16, the power shape of ULPU-V has a smaller peak heat flux region, but the heating power at 85°–90° is lacked. The SF-72-0.5 and T40B have different power shapes,  $P_{upstream}$  and  $P_{downstream}$ . In the comparison of these two different experiments, the effect of heat flux distribution can be further studied.

Though the experiments in this paper and ULPU-V experiments are quite different, the CHF results are similar at 70°. The results in these experiments are shown in Table 3.

In general, the results of SF-72-0.5 and T40B are similar such as CHF, flow rate, and total power at 0–84°. These two different experiments did not show different flow characteristics and CHF. The difference of pressure drops is caused by the different heights of flow passage (2622 mm of experiments in this paper and 1703 mm of ULPU-V). The total power of SF-72-0.5 is 1.4 times the total power of T40B in ULPU-V. However, the total powers at 0–84° of SF-72-0.5 and T40B are similar. All these different issues do not affect the CHF at 70°.

#### 4. Conclusions

In this paper, a series of experiments under IVR-ERVC conditions were conducted to study the effect of heat flux distribution on CHF. In the experiments, the full-height modular facility is used. Several issues (such as molten pool configurations and upstream and downstream heating power) are chosen to take 4 test cases. After analysis and discussion, the experimental results can be summarized as follows:

- (1) As the power shapes used in experiments change with different test angles, the natural circulation flow characteristics are not obviously affected. At two different THP, the pressure drops in the flow passage are similar for all the 6 test angles.
- (2) For test cases 2 and 3, the upstream heating power and downstream heating power are changed, respectively. These heat flux distributions can only lead to a little more steps of increasing heating power during experimental process, which means a larger  $q_{CHF,apparent}$ . After the thermal equilibrium calculation, the results of  $q_{CHF}$  are all similar. The relative deviations are less than 5%.
- (3) For molten pool configuration experiments in test cases 1 and 4, the difference of normalized power shapes is just upstream and downstream heating power, which is similar to the test cases 2 and 3. Therefore, the flow characteristics and CHF are

similar in test cases 1 and 4. Only the CHF values of 81° and 87° cases in the three-layer configuration experiments are a little lower probably affected by the focus effect. However, this deviation is quite minimal. The relative deviations of CHF are less than 3%. The two-layer configuration experiments are compared with ULPU-V experiments which used a different two-layer molten pool power shape. After analysis, there is no obvious difference of the results in these two experiments.

- (4) Considering all the above analyses, the boiling crisis is mainly triggered by the local thermal hydraulics parameters. The CHF of RPV external wall is not obviously affected by the heat flux distribution of molten pool. The varying heat flux distribution of the transients in the lower head will not threaten the success of IVR strategy.

#### Data Availability

The data used to support the findings of this study are included within the article.

#### Conflicts of Interest

The authors declare that there are no conflicts of interest regarding the publication of this paper.

#### Acknowledgments

The authors would like to thank all members of the IVR joint research group of SJTU (Shanghai Jiao Tong University) and SNERDI (Shanghai Nuclear Engineering Research and Design Institute) for their contributions to this paper. This study was financially supported by the China National Major Project of Science and Technology for Large Advanced PWR (no. 2018ZX06002004-003).

#### References

- [1] T. G. Theofanous and C. Liu, *In-Vessel Coolability and Retention of a Core Melt*, 1996.
- [2] O. Kymäläinen, H. Tuomisto, and T. Theofanous, "In-vessel retention of corium at the Loviisa plant," *Nuclear Engineering and Design*, vol. 169, pp. 109–130, 1997.
- [3] T. Theofanous, C. Liu, and S. Additon, *In-Vessel Coolability and Retention of a Core Melt*, Department of Energy Report, Washington, USA, 1996.
- [4] W. Ma, Y. Yuan, and B. R. Sehgal, "In-vessel melt retention of pressurized water reactors: historical review and future research needs," *Engineering*, vol. 2, no. 1, pp. 103–111, 2016.

- [5] H. Esmaili and M. Khatib-Rahbar, *Analysis of In-Vessel Retention and Ex-Vessel Fuel Coolant Interaction for AP1000*, Energy Research, Inc., Rockville, MA, USA, 2004.
- [6] S. J. Oh and H. T. Kim, "Effectiveness of external reactor vessel cooling (ERVC) strategy for APR1400 and issues of phenomenological uncertainties," in *Workshop Proceedings: Evaluation of Uncertainties in Relation to Severe Accidents and Level-2 Probabilistic Safety Analysis*, Aix-en-Provence, France, 2005.
- [7] J. Xing, D. Song, and Y. Wu, "HPR1000: advanced pressurized water reactor with active and passive safety," *Engineering*, vol. 2, no. 1, pp. 79–87, 2016.
- [8] S. Rougé, "SULTAN test facility for large-scale vessel coolability in natural convection at low pressure," *Nuclear Engineering and Design*, vol. 169, no. 1–3, pp. 185–195, 1997.
- [9] V. Asmolov, "Latest findings of RASPLAV project," in *Proceedings of the Workshop on In-Vessel Core Debris Retention and Coolability*, OECD/CSNI/NEA, Munich, Germany, March, 1998.
- [10] S. Bechta and V. Asmolov, "Zr partitioning tests in the cold crucible test MA-1," in *Proceedings of the OECD MASCA Meeting*, Helsinki, Finland, April, 2001.
- [11] J. L. Rempe, D. L. Knudson, C. M. Allison et al., *Potential for AP600 In-Vessel Retention through Ex-Vessel Flooding*, INEEL, USA, 1997.
- [12] J. Weisman and B. S. Pei, "Prediction of critical heat flux in flow boiling at low qualities," *International Journal of Heat and Mass Transfer*, vol. 26, no. 10, pp. 1463–1477, 1983.
- [13] B. Kuang, P. Liu, F. Wang, K. Cao, and K. Zhang, "Influences of some engineered factors on IVR-ERVC limits," *Nuclear Engineering and Design*, vol. 347, pp. 20–30, 2019.
- [14] B. Kuang and P. F. Liu, "Study on full-size tests of critical heat flux on lower head outer wall and duct flow for cap1400 ervc strategy," Scientific Report, Shanghai Jiao Tong University, Shanghai, China, 2014.
- [15] P. F. Liu and B. Kuang, "The comprehensive validation platform of full-height cap1400 passive ervc circulating flow and heat transfer tests," Scientific Report, Shanghai Jiao Tong University, Shanghai, China, 2014.
- [16] Z. Cao and J. Wang, "IVR analysis code development and validation based on three-layer melt pool configuration," *Atomic Energy Science and Technology*, vol. 52, no. 5, pp. 912–919, 2018.
- [17] K. Ge, Y. P. Zhang, W. X. Tian, G. H. Su, and S. Z. Qiu, "Effect of stratified interface instability on thermal focusing effect in two-layer corium pool," *International Journal of Heat and Mass Transfer*, vol. 133, pp. 359–370, 2019.
- [18] Y. Zhou, S. Wu, Y. Zhang et al., "Experimental research on heat transfer behavior of large scale two-layer salt melt pool based on COPRA facility," *Annals of Nuclear Energy*, vol. 138, p. 107166, 2020.
- [19] Y. B. Li, L. L. Tong, X. W. Cao, and D. Q. Guo, "In-vessel retention coolability evaluation for Chinese improved 1000 MWe PWR," *Annals of Nuclear Energy*, vol. 76, pp. 343–349, 2015.
- [20] T. N. Dinh, J. P. Tu, and T. Salmassi, *Limits of Coolability in the AP1000-Related ULPU-2400 Configuration V Facility*, 2003.